Available online at www.sciencedirect.com

ScienceDirect

Procedia Computer Science 271 (2025) 51–57

Procedia Computer Science

www.elsevier.com/locate/procedia

International Conference on Biomimetic Intelligence and Robotics 2025

Design and Analysis of a Flapping-Wing Aircraft with Multi-Degree-of-Freedom Deformable Tail and Wing

Longtian Zhang[a,b], Hao Liu[a], Kaicheng Yu[a], Qiukai Zhao[a], Yonglong Bi[a], Chao Wang[a,b,*]

[a]School of Mechanical Engineering, DongGuan University of Technology, Dongguan, China
[b]Dongguan Key Laboratory of Intelligent Bionic Robot Technology and System, Dongguan, China

Abstract

To enhance the flight performance of a flapping-wing aircraft and achieve bird-like foldable wing-tail motion, this study designs an ornithopter featuring a deformable wing mechanism and a multi-degree-of-freedom tail mechanism. Through kinematic analysis and calculations, parametric design was conducted for both the deformable wing mechanism and the multi-degree-of-freedom tail mechanism. The motion trajectory and characteristics of the wing mechanism were validated using ADAMS. Subsequently, the simplified 3D model of the prototype was imported into ANSYS Fluent to compute the aerodynamic loads acting on the vehicle. Structural integrity assessment of critical load-bearing components was performed via strength analysis in ANSYS Workbench. This research provides a theoretical foundation and technical support for the design and development of ornithopters.

Keywords: Flapping-Wing Aircraft; Structural Design; Kinematic Analysis; Finite Element Analysis

1. Introduction

For a long time, the remarkable flight capabilities of birds and insects in nature have continuously inspired human exploration of unmanned aerial vehicles. However, to this day, the impressive flight maneuverability exhibited by birds remains significantly superior to that of artificial aircraft, particularly when the Reynolds number decreases below 10^5. Under such conditions, birds continue to demonstrate superior flight maneuverability and adaptability compared to man-made aircraft [1, 2, 3]. Existing research indicates that birds achieve active control over both longitudinal and lateral flight by simultaneously altering the configurations of their wings and tail during flight [4, 5]. The synergistic motion of the wings and tail not only enhances the birds' aerodynamic performance but also ensures balance during climbing, gliding, and turning maneuvers, thereby increasing flight agility [6, 7, 8, 9, 10, 11, 12].

In recent years, there has been considerable research on bio-inspired aerial vehicles based on wing-tail cooperative motion. Phan et al. [13] developed a biomimetic feathered vehicle, "LisRaptor," in 2024, mimicking the skeletal and feather structure of raptors. Their work further demonstrated that a cooperatively deformable wing-tail structure can enable sharp turns with small radii and revealed the core aerodynamic function of the avian tail during turning flight.

* Corresponding author.
E-mail address: wangchao@dgut.edu.cn

10.1016/j.procs.2025.10.110

In the same year, Chang et al. [14], aiming to address issues of sustained autonomous flight and stability control in bird-like aircraft, developed a bio-inspired vehicle with morphing wings and tail, named "PigeonBot II." This vehicle achieved stable suppression of Dutch roll oscillations by combining asymmetric wing folding with coordinated tail tilting and lateral deflection, thereby inhibiting roll motion and yaw disturbances.

While the aforementioned research on aerial vehicles has achieved structural motion effects analogous to the folding and unfolding of avian wings and tails, most are fixed-wing vehicles rather than ornithopters. Consequently, they cannot fully replicate the folding wing-tail motion characteristic of birds during flapping flight. Within existing ornithopter research, although several vehicles with foldable wing structures have been developed – such as the foldable-wing ornithopter by Stowers et al. [15] and the "Little Falcon" ornithopter by Chen et al. [16] – their tail structures typically adopt T-shaped or V-shaped configurations. These designs are generally incapable of achieving the multi-degree-of-freedom (MDOF) motion characteristic of avian tails.

Therefore, this paper presents the design of an ornithopter featuring a multi-degree-of-freedom foldable wing-tail mechanism. As shown in Fig.1, the wings can fold and unfold during flapping, while the tail structure can perform bird-like motions including twisting, pitching, yawing, and folding/unfolding. Kinematic analysis methods were employed to establish the relationship between the geometric parameters of each component and the resulting output motion. Furthermore, ADAMS and ANSYS were utilized to validate the motion characteristics and structural reliability of the designed wing and tail mechanisms.

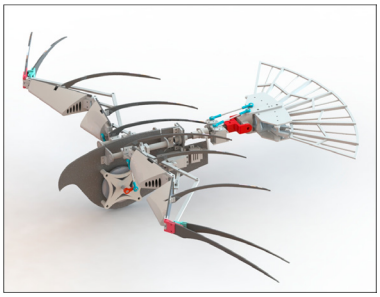

Fig. 1. Schematic diagram of the three-dimensional model of the flapping-wing aircraft prototype

2. Wing and tail mechanism design

2.1. Wing mechanism design

The simplified schematic of the wing mechanism is presented in Fig. 2. The primary structure of this mechanism consists of two planar four-bar linkages and one slider-rocker mechanism. In this configuration, links OD, DG, and GH correspond to the humerus, radius, and metacarpal bone within the avian wing skeleton, respectively. The angles θ_s, θ_e, and θ_w represent the shoulder joint angle, elbow joint angle, and wrist joint angle of the avian wing skeleton accordingly. By driving the slider along the X-axis, it is possible to actuate the entire wing mechanism to perform extension and folding movements along the Y-direction with a defined motion.

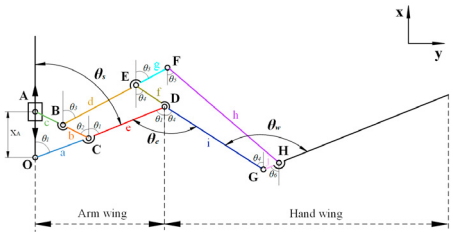

Fig. 2. Foldable Wing Mechanism Schematic

Furthermore, conducting a kinematic analysis of the wing mechanism necessitates establishing a kinematic model. This model will investigate the relationship between slider displacement distance (X_A) and the angles at which both shoulder joint (θ_s), elbow joint (θ_e), and wrist joint (θ_w) are positioned as well as various link lengths in both fully extended and fully folded states of the wing mechanism. Schematic diagrams illustrating these two configurations are provided in Fig 3 below; specifically, Fig 3a depicts the mechanism in its fully extended configuration while Fig 3b illustrates it in its fully folded state.

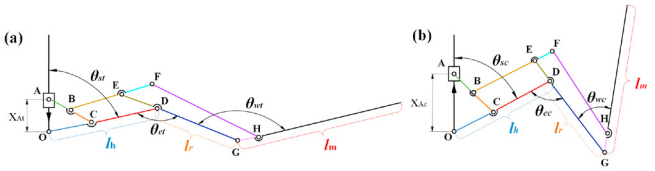

Fig. 3. (a) Schematic Diagram of the Fully Deployed Mechanism; (b) Schematic Diagram of the Fully Folded Mechanism

As shown in Fig. 3, an independent analysis is conducted on both slider-rocker mechanisms and planar four-bar linkages. This analysis yields vector loop equations relevant to each link involved.

$$\overrightarrow{OA} = \overrightarrow{OC} + \overrightarrow{CA} \tag{1}$$

$$\overrightarrow{CB} + \overrightarrow{BE} + \overrightarrow{ED} + \overrightarrow{DC} = 0 \tag{2}$$

$$\overrightarrow{EF} + \overrightarrow{FH} + \overrightarrow{HG} + \overrightarrow{GE} = 0 \tag{3}$$

As illustrated in Fig 2 and Fig 3, the shoulder joint angle (θ_s), elbow joint angle (θ_e), wrist joint angle (θ_w), humerus (l_h), and radius (l_r) are defined as follows:

$$\begin{cases} \theta_s = \theta_1; \theta_e = \theta_1 + \theta_4; \theta_w = \theta_4 + \theta_6 \\ l_h = a + e; l_r = i \end{cases} \tag{4}$$

Equations (1), (2), and (3) are orthogonally decomposed along the x-y direction. Subsequently, the data presented in Equation (4) are substituted into the respective decomposed formulas. By employing trigonometric relationships, it is possible to eliminate the variables, resulting in:

$$(x_A - (l_h - e)cos\theta_s)^2 + (l_h - e)^2\, sin^2\theta_s = (b + c)^2 \tag{5}$$

$$(ecos\theta_s + fcos(\theta_e - \theta_s) - b\frac{x_A - (l_h - e)cos\theta_s}{b + c})^2 + \left(esin\theta_s - fsin\,(\theta_e - \theta_s) + b\frac{(l_h - e)\,sin\theta_s}{b + c}\right)^2 = d^2 \tag{6}$$

$$\begin{aligned} &(\frac{g}{d}(ecos\theta_s + fcos(\theta_e - \theta_s) - b\frac{x_A - (l_h - e)cos\theta_s}{b + c}) - jcos(\theta_w - \theta_e + \theta_s) + (l_r + f)cos(\theta_e - \theta_s))^2 \\ &+ (\frac{g}{d}(esin\theta_s - fsin(\theta_e - \theta_s) + b\frac{(l_h - e)sin\theta_s}{b + c}) + jsin(\theta_w - \theta_e + \theta_s) + (l_r + i)sin(\theta_e - \theta_s))^2 = h^2 \end{aligned} \tag{7}$$

Based on the design requirements of the aircraft examined in this study, the parameters depicted in the figures are detailed in Table 1 as follows.

By substituting the parameters outlined in Table 1 into Equations (5), (6), and (7), we can establish the state equations for the wing mechanism in both extended and folded configurations. These equations facilitate solving for the remaining six unknown variables. Following computation and consideration of practical machining precision requirements, the designed link lengths of the wing mechanism are presented in Table 2.

Table 1. Wing Mechanism Parameters

Basic Parameters	Fully Extended State	Fully Folded State
l_h = 165 mm	θ_{st} = 78°	θ_{sc} = 61°
l_r = 176 mm	θ_{et} = 138°	θ_{ec} = 120°
l_m = 291 mm	θ_{wt} = 122°	θ_{wc} = 59°
b = 56.8 mm	x_{At} = 37 mm	x_{Ac} = 62 mm
g = 65 mm		

Table 2. The length of each rod of the wing mechanism

l_{AC}	l_{BF}	l_{OD}	l_{EG}	l_{FH}	l_{GH}
81.8 mm	160 mm	146.49 mm	230.47 mm	200.27 mm	18.92 mm

Based on the parameters of each rod length and angle outlined in the aforementioned formulas, a three-dimensional model was constructed and imported into ADAMS simulation software to analyze the motion relationship between the slider displacement (X_A) and the shoulder joint angle (θ_s), elbow joint angle (θ_e), and wrist joint angle (θ_w). The slider was programmed to slide uniformly along the guide rod at a speed of 1 mm/s for a duration of 25 seconds, after which it returned to its original position at the same speed.

The results illustrating the variation relationship between the slider displacement and each wing joint angle during this process are presented in Fig.4(b). It is evident that as the wing undergoes folding and extending movements, all joint angles initially decrease before subsequently increasing. Notably, while both shoulder joint angle and elbow joint angle exhibit relatively stable changing speeds, there is a significant alteration in the tangent slope of the wrist joint angle curve when slider displacement ranges from 15 mm to 25 mm.

Additionally, a reference point was established at the wingtip to further analyze the motion trajectory during flapping. As depicted in Fig. 4(a), this trajectory demonstrates that by synchronizing the reciprocating motion of the slider with flapping action, the wing mechanism successfully achieves an "O"-shaped flapping path as intended.

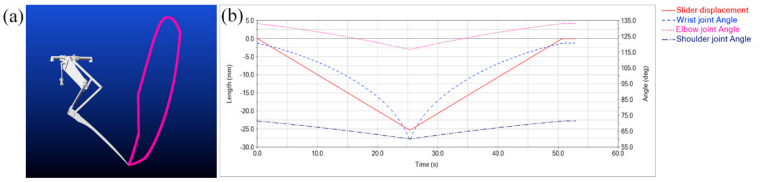

Fig. 4. (a)Wing tip movement trajectory; (b)Kinematic Relationship Plot between Slider Displacement (X_A) and Joint Angles (θ_s,θ_e,θ_w)

2.2. Tail mechanism design

To achieve a bio-inspired multi-degree-of-freedom tail mechanism comparable to avian morphology, this study integrates a gimbal structure with a cable-driven system, utilizing three servo motors to independently control the pitch, twist, and yaw motions of the tail mechanism. The kinematic schematic governing pitch and yaw control is presented in Fig.5, where Fig.5(b) shows the top view of the motion model, while Fig.5(a) and Fig.5(c) depict the right-side and left-side views respectively.Points A and B represent the rotation axes of the two servo cranks, where d denotes the distance from the servo rotation axes to the center O.

As shown in Fig.5(b), within the left and right closed-loop areas corresponding to servo A and servo B respectively, based on the vector relationship among each member, it can be obtained.

$$\begin{cases} \overrightarrow{OC} = \overrightarrow{OA} + \overrightarrow{AC}; \overrightarrow{OD} = \overrightarrow{OK} + \overrightarrow{KD}; \overrightarrow{CD} = \overrightarrow{OD} - \overrightarrow{OC} \\ \overrightarrow{OJ} = \overrightarrow{OB} + \overrightarrow{BI} + \overrightarrow{IJ}; \overrightarrow{OK} = \overrightarrow{OG}; \overrightarrow{KJ} = \overrightarrow{OJ} - \overrightarrow{OK} \end{cases} \tag{8}$$

Based on the vector relationship in equation (8), the spatial coordinates of points C, D, J, and K are determined. According to the rod length calculation formula, the relational expressions between each rod length and angle in equation (9) can be derived. Meanwhile, based on the actual rod length measurement, it is formulated that $l_1 = 90.79$ mm; $l_2 = 80.85$ mm.

$$\begin{cases} l_1^2 = [a_r \cdot \sin(\theta_a - \varphi_a) - h - r_w \cdot \cos(a_w + \lambda_w)]^2 + [-e_w + n_w]^2 \\ \quad +[d + a_r \cdot \cos(\theta_a - \varphi_a) + r_w \cdot \sin(a_w + \lambda_w)]^2 \\ l_2^2 = [b_r \cdot \sin(\theta_b - \varphi_b) - h]^2 + [b_r \cdot \cos(\theta_b - \varphi_b)]^2 + [-e_w + n_w]^2 \\ l_2^2 = 0.79 l_1^2 \end{cases} \tag{9}$$

Here, a_r and b_r are the crank lengths of the left and right steering gears A and B, respectively; θ_a and θ_b are the initial angles of the cranks of steering gears A and B, respectively; φ_a and φ_b are the rotation angles of the cranks of steering gears A and B, respectively; r_w is the length of the rocker DK; a_w is the angle between the rocker DK and the central axis of the empennage; λ_w, ϕ_w and ϕ_0 are the yaw angle, pitch angle and initial pitch angle, respectively. Among them, the steering gear rotation angles φ_a and φ_b correspond to the control of the pitch angle ϕ_w and yaw angle λ_w in the empennage mechanism, respectively.

Considering practical machining precision and aircraft manufacturing requirements, the link lengths and initial angle parameters are determined as shown in Table 3.

Table 3. Basic parameters

Basic parameters			
$m_w = 20.7$ mm	$l_1 = 90.79$ mm	$l_2 = 80.85$ mm	$a_r = 7$ mm
$b_r = 7$ mm	$\theta_a = 13.4°$	$n_w = 27.16$ mm	$h = 78.15$ mm
$e_w = 16.96$ mm	$\phi_0 = 23.84°$	$\theta_b = 53°$	$\alpha_w = 53.5°$
$r_w = 23.8°$			

The twisting and spreading motions of the tail mechanism are directly actuated via servo motors and a cable-driven system, with the detailed 3D model illustrated in Fig.5(d).

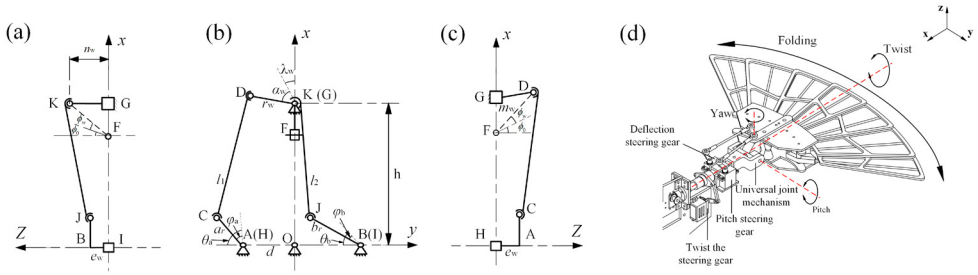

Fig. 5. Tail Mechanism Kinematic Schematic and 3D model illustrated

2.3. *Computational Fluid Dynamics Simulation*

To further validate the flight performance of the designed wing and empennage mechanisms (Fig.6), a simplified 3D model of the aircraft prototype was imported into ANSYS Fluent for computational analysis. Using the SST k-ω turbulence model and overset grid method, with airflow velocity at 5 m/s, wing flapping frequency at 5 Hz, flapping angle at 58° (20° upstroke, 38° downstroke), and average angle of attack at 0°, the lift and thrust variation curves during level flight under these conditions were obtained (Fig.7 and 8).

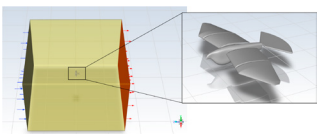

Fig. 6. Flapping-wing aircraft Simulation Models

As illustrated in Fig.7, Fig.7(a) and 7(b) depict the lift forces generated by the wings and the tail over two cycles. The trends observed in these forces correspond to the flutter behavior of the aircraft, with the lift force produced by the wings significantly exceeding that of the tail.

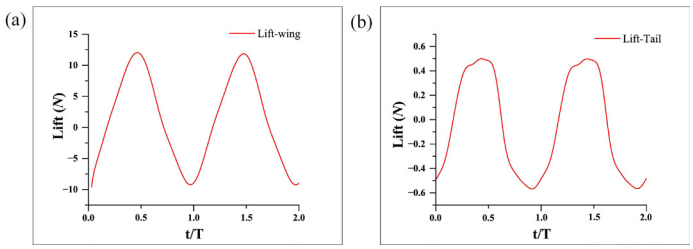

Fig. 7. Lift Variation Curve

Fig.8(a) and Fig.8(b) illustrate the thrust produced by the wings and tail over two cycles, respectively. The variation patterns of these two components within a single cycle exhibit inconsistencies. Notably, throughout a single cycle, the thrust generated by the wings consistently demonstrates positive values.

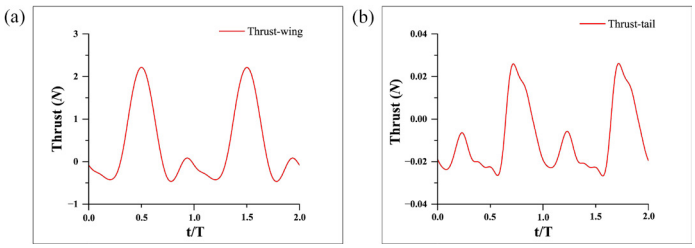

Fig. 8. Thrust Variation Curve

2.4. Workbench Mechanics Simulation

Based on the aerodynamic load data obtained from fluid simulations, a mechanical simulation analysis was conducted on the force-bearing components at the joints of both the wing mechanism and tail mechanism.

As illustrated in Fig. 9, the component in question is a fixed part at the wing tip, made of aluminum alloy. A time-varying lift load (defined by the lift curve) and a static load of 0.98 N acting downward along the y-axis (perpendicular to the ground) were applied to its upper surface to simulate the lift force and the wing's own weight during the aircraft's flapping motion.As shown in Fig. 9(a), the maximum equivalent stress occurs at the middle fillet, with a value of 0.88 MPa. Fig. 9(b) indicates that the maximum deformation in the y-direction is 0.00044 mm. The results demonstrate that both the deformation and stress of this component are within the allowable limits of the material strength

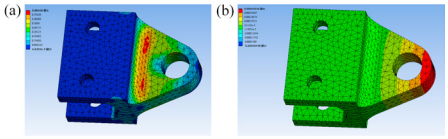

Fig. 9. (a) Equivalent stress of the wing terminal connector, (b) Directional deformation of the wing terminal connector

As shown in Fig.10, the wing link, made of aluminum alloy, is used to transmit the folding motion of the wing. A time-varying lift load (defined by the wing lift curve) was applied to its upper surface. The results in Fig. 10(a) show that the maximum equivalent stress of the wing link occurs at the joint of the circular holes at both ends, with a value of 12.43 MPa, while Fig.10(b) indicates that the maximum deformation of the wing link in the y-axis is located in the middle of the link, measuring 0.075 mm. These results demonstrate that both the deformation and stress of the part are within the allowable limits of the material strength.

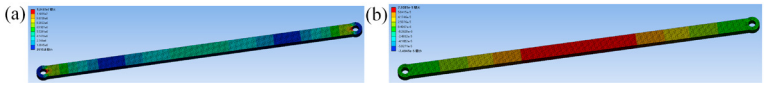

Fig. 10. (a) Equivalent stress of the wing connecting rod, (b) Directional deformation of the wing connecting rod

As shown in Fig. 11, the tail carbon fiber hollow tube is made of carbon fiber (with a modulus of 230 GPa). A time-varying lift load (defined by the tail lift curve) and a static load of 1 N acting downward along the y-axis (perpendicular to the ground) were applied to its right upper surface. As depicted in Fig. 11(a), the maximum stress of the part is located in the middle of the hollow tube, with a value of 0.274 MPa. As shown in Fig. 11(b), the maximum deformation of the hollow tube occurs at the right loaded end, measuring 0.00028 mm. The results indicate that both the deformation range and stress intensity of the tail carbon fiber hollow tube meet the strength requirements of the tail mechanism.

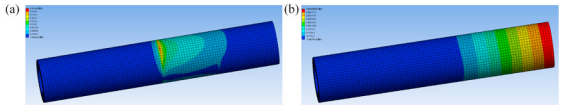

Fig. 11. (a) Equivalent stress of the tail carbon fiber hollow tube, (b) Directional deformation of the tail carbon fiber hollow tube

3. Conclusion

When birds are in flight, they frequently attain enhanced maneuverability and stability through the coordinated movement of their wings and tails. In this study, a flapping-wing aircraft equipped with multi-degree-of-freedom deformable wings and tails is designed, with a focus on the design and analysis of the wing and tail mechanisms.

Firstly, the kinematic equations for both the wing mechanism and the tail mechanism were derived, and the corresponding rod length and angle parameters were configured. The motion characteristics of the wing mechanism were simulated and analyzed using ADAMS software. Subsequently, the three-dimensional model of the aircraft was simplified and imported into ANSYS Fluent to perform three-dimensional fluid simulation calculations. The lift variation curves and thrust variation curves of the wing mechanism and tail mechanism were obtained respectively. Based on the aerodynamic data derived from the fluid simulation calculations, ANSYS Workbench was employed to analyze the stress and deformation of the load-bearing components at the joints of the wing mechanism and tail mechanism, thereby further verifying the feasibility of the designed wing mechanism and tail mechanism.

Acknowledgements

This work supported in part by the GuangDong Basic and Applied Basic Research Foundation (2024A1515140103, 2022A1515140043) and in part by the College Students' Innovation and Entrepreneurship Training Program of DGUT (202411819091, 202511819025)

References

[1] Harvey C, Inman D J. Aerodynamic efficiency of gliding birds vs. comparable UAVs: a review[J]. Bioinspiration & Biomimetics, 2020.

[2] Shyy, W., Aono, H., Chimakurthi, S. K., Trizila, P., Kang, C. K., Cesnik, C. E., & Liu, H. (2010). Recent progress in flapping wing aerodynamics and aeroelasticity[J]. Progress in Aerospace Sciences, 46(7), 284-327.

[3] Bayiz, Y., Ghanaatpishe, M., Fathy, H., & Cheng, B. (2018). Hovering efficiency comparison of rotary and flapping flight for rigid rectangular wings via dimensionless multi-objective optimization[J]. Bioinspiration & biomimetics, 13(4), 046002.

[4] entink D, Müller U K, Stamhuis E J, et al. How swifts control their glide performance with morphing wings[J]. Nature, 2007, 446(7139): 1082-1085.

[5] Thomas A L R, Taylor G K. Animal Flight Dynamics I. Stability in Gliding Flight[J]. Journal of Theoretical Biology, 2001, 212(3): 399-424.

[6] Usherwood J R, Cheney J A, Song J, et al. High aerodynamic lift from the tail reduces drag in gliding raptors[J]. Journal of Experimental Biology, 2020, 223(3): jeb214809.

[7] Thomas A L R. The Flight of Birds that have Wings and a Tail: Variable Geometry Expands the Envelope of Flight Performance[J]. Journal of Theoretical Biology, 1996, 183(3): 237-245.

[8] Thomas AL. On the aerodynamics of birds' tails[J]. Philosophical Transactions of the Royal Society of London. Series B: Biological Sciences. 1993 Jun 29;340(1294):361-80.

[9] ucker V A. Pitching Equilibrium, Wing Span and Tail Span in a Gliding Harris' Hawk, Parabuteo Unicinctus[J]. Journal of Experimental Biology, 1992, 165(1): 21-41.

[10] Glenn, R., Dahlke, L. B., Engilis Jr, A., & Harvey, C. (2024). Analysis of bird wing airfoil aerodynamic efficiency[J]. In AIAA SCITECH 2024 Forum (p. 1127).

[11] Rosén, M., & Hedenström, A. (2001). Gliding flight in a jackdaw: a wind tunnel study[J]. Journal of Experimental Biology, 204(6), 1153-1166.

[12] KleinHeerenbrink, M., & Hedenström, A. (2017). Wake analysis of drag components in gliding flight of a jackdaw (Corvus monedula) during moult[J]. Interface focus, 7(1), 20160081.

[13] Phan H-V, Floreano D. A twist of the tail in turning maneuvers of bird-inspired drones[J]. Science Robotics, 2024, 9(96): eado3890.

[14] Chang E, Chin D D, Lentink D. Bird-inspired reflexive morphing enables rudderless flight[J]. Science Robotics, 2024, 9(96): eado4535.

[15] Stowers A K, Lentink D. Folding in and out: passive morphing in flapping wings[J]. Bioinspiration & biomimetics, 2015, 10(2): 025001.

[16] Chen, A., Song, B., Wang, Z., Xue, D., & Liu, K. (2022). A novel actuation strategy for an agile bioinspired FWAV performing a morphing-coupled wingbeat pattern[J]. IEEE Transactions on Robotics, 39(1), 452-469.